

# **A numerical parametric study of the mechanical action of pulsatile blood flow onto axisymmetric stenosed arteries**

Tristan Belzacq<sup>\*†</sup>, Stéphane Avril<sup>†</sup> Emmanuel Leriche<sup>□</sup> and Alexandre Delache<sup>‡</sup>

**\*Corresponding author**

Email: belzacq@emse.fr

<sup>†</sup>Ecole Nationale Supérieure des Mines, Centre Ingénierie et Santé, CNRS UMR 5146, 158  
cours Fauriel, 42023 Saint-Etienne cedex 2, France

<sup>□</sup> Laboratoire de Mécanique de Lille, Université de Lille, Avenue Paul Langevin, Cité  
Scientifique, F-59655 Villeneuve d'Ascq cedex, France

<sup>‡</sup> Laboratoire de Mécanique des fluides et d'acoustique LMFA, site de St-Etienne, Université  
de Lyon, F-42023 St-Etienne, France, Université Jean Monnet de St-Etienne, Faculté des Sciences  
et Techniques, 23 rue du Docteur Paul Michelon, 42023 St-Etienne cedex 2, France

## Abstract

In the present paper, a fluid structure interaction model is developed, questioning how the mechanical action of the blood onto an atheromatous plaque is affected by the length and the severity of the stenosis. An axisymmetric model is considered. The fluid is assumed Newtonian. The plaque is modelled as a heterogeneous hyperelastic anisotropic solid composed of the arterial wall, the lipid core and the fibrous cap. Transient velocity and pressure conditions of actual pulsatile blood flow are prescribed. The simulation is achieved using the Arbitrary Lagrangian Eulerian scheme in the COMSOL commercial Finite Element package. The results reveal different types of behaviour in function of the length (denoted  $L$ ) and severity (denoted  $S$ ) of the stenosis. Whereas large plaques ( $L > 10\text{mm}$ ) are mostly deformed under the action of the blood pressure, it appears that shorter plaques ( $L < 10\text{mm}$ ) are significantly affected by the shear stresses. The shear stresses tend to deform the plaque by pinching it. This effect is called: “the pinching effect”. It has an essential influence on the mechanical response of the plaque. For two plaques having the same radius severity  $S=45\%$ , the maximum stress in the fibrous cap is 50% larger for the short plaque ( $L=5\text{mm}$ ) than for a larger plaque ( $L=10\text{mm}$ ), and the maximum wall shear stress is increased of 100%. Provided that they are confirmed by experimental investigations, these results may offer some new perspectives for understanding the vulnerability of short plaques.

**Keywords:** vascular biomechanics; fluid structure interaction; numerical simulation; stenosis; blood flow

51	<b>Global variables:</b>
52	
53	$\rho$ the density
54	$\eta$ the viscosity
55	$R_0$ the healthy arterial radius
56	$h_0$ the thickness of the healthy arterial wall
57	$e$ the fibrous cap thickness
58	$L$ the stenosis length
59	$R_m$ the external stenosis remodelling radius
60	$S$ the stenosis severity in terms of diameter
61	$S_{area}$ the stenosis severity in terms of area
62	$(\alpha_k)_k$ the series of Womersley number
63	$\mathbf{e}_z$ the longitudinal axis in the cylindrical frame
64	$\mathbf{e}_r$ the radial axis in the cylindrical frame
65	$\mathbf{n}$ exterior normal
66	$\mathbf{u}$ the displacement vector
67	$\mathbf{v}$ the velocity
68	$p$ the pressure
69	$\boldsymbol{\sigma}$ the stress tensor
70	$\mathbf{F}$ the deformation gradient tensor
71	$\mathbf{C}$ the Green-Cauchy right strain tensor
72	$\varphi$ the strain energy density
73	$J$ the volume change invariant
74	$I_1, I_4$ and $I_6$ the first, fourth and sixth coordinate invariants
75	$c, k_1$ and $k_2$ the parameters of the Holzapfel model
76	$\beta$ the angle between these two fibres family
77	$\mathbf{M}$ and $\mathbf{M}'$ the direction's vectors of the two fiber's family in the cylindrical coordinate
78	$\mathbf{w}$ the mesh velocity in the Arbitrary Lagrangian Eulerian scheme
79	$\tau$ the wall shear stress
80	$\varepsilon_R$ the average radial strain of the plaque
81	$\gamma$ the average shear strain of the plaque
82	$U_r$ the radial displacement component of the fibrous cap at the middle of the stenosis
83	$U_z$ the longitudinal displacement of the fibrous cap at the middle of the stenosis
84	$P_1$ the linear type of finite elements
85	$P_2$ the quadratic type of finite elements
86	$\Omega$ a domain
87	$\partial\Omega$ a boundary
88	
89	<b>Indexes:</b>
90	
91	$s$ the solid part
92	$f$ the fluid part
93	$fs$ fluid-structure
94	$i$ the material number ( $1 \leq i \leq 4$ )
95	$in$ inlet

96 *out* outlet  
 97 *ext* exterior  
 98 *sym* symmetric  
 99 *max* maximum  
 100  
 101 **Operators:**  
 102  
 103  $\det(\cdot)$  the determinant of a tensor  
 104  $\frac{\partial}{\partial t}$  the first derivative with respect to time  
 105  $\frac{\partial^2}{\partial t^2}$  the second derivative with respect to time  
 106  $\nabla \cdot$  the divergence operator  
 107  $\nabla$  the gradient operator  
 108  $\mathbf{I}$  the identity matrix  
 109  ${}^t\mathbf{A}$  transpose of the matrix  $\mathbf{A}$   
 110  $Re(\cdot)$  the real part of an imaginary number  
 111  $J_0(\cdot)$  the zero order Bessel function of first kind  
 112  
 113

## 114 1. Introduction

115

116 The fracture of vulnerable carotid atherosclerotic plaques is the major cause of  
 117 cerebrovascular thromboembolic events such as strokes and ischemic attacks [1]. The  
 118 vulnerability is believed to be related to mechanical forces, vessel surface condition, cell  
 119 activities and chemical environment [2-4].

120

121 In current clinical practice, carotid endarterectomy is the most frequently used treatment for  
 122 pathological plaques. The decision leading to surgery is based on the degree of endoluminal  
 123 stenosis [5,6]. But this criterion alone is insufficient to predict the plaque fracture and the  
 124 necessity to identify other criteria is a major issue for public health [1]. Therefore, there is a  
 125 strong medical and economical interest in developing new tools for a better understanding of  
 126 this situation.

127

Histological studies have related plaque vulnerability with thin fibrous cap, large necrotic core [2] and inflammation after macrophages or T-cells infiltration in the lipid core [3] or foam cells infiltration in the fibrous cap [4]. Advanced magnetic resonance imaging (MRI) allows *in vivo* virtual histology of plaques [7,8].

There has also been considerable effort using computational models to perform mechanical analysis for atherosclerotic plaques and identify critical mechanical descriptors as stresses or strains related to plaque rupture. There is no universal technique that can measure the strain/stress field in the plaque but it is widely believed that stress concentration in the fibrous cap of vulnerable plaques can cause the rupture [9,10]. Large cyclic variations of strain/stress may also lead to artery fatigue [11-13]. Several studies, for example, indicate that the critical strain/stress conditions are affected by the stenosis severity, the lipid pool size, the fibrous cap thickness and the stenosis eccentricity [14-17].

2-D and 3-D patient-specific finite-element (FE) models of diseased vessels are probably the best way to obtain stress distributions for specific plaques. The models are based on histology or pre-fracture medical imaging [18]. Their purpose is to associate the mechanical descriptors to the mechanical process of plaque rupture.

Nevertheless the sparsity of data regarding plaque rupture reveals the limitations of the predictive models. The models may be:

- fluid models [19-21] with rigid plaques
- 2D solid models under pressure loads [14,22-26] considering cross sections of idealized plaques

- or fluid structure interaction (FSI) models taking into account both the combination of shear and pressure loads [9,10,18,27-33].

FSI models are probably the most realistic models but their models are complex. The interaction between the blood flow and the plaque is not yet fully understood, especially due to the large variability of plaques [8]. Using idealized models allows investigating how the mechanical action of the blood onto the plaque is affected by the geometry and the mechanical properties. For instance, Li Z.Y. et al. [15] studied the influence of stenosis severity and fibrous cap thickness on stresses in plaques with 2D plane-strain models. Li M.X. et al. [16] investigated the stress distribution for different degrees of stenoses also with 2D-axisymmetric models. Valencia et al. [34] investigated the influence of the severity of stenoses on stresses with 3D-axisymmetric models. Tang et al. performed many 3D FSI studies on idealized plaque models. They analysed wall stress and strain in symmetric and asymmetric plaque models with two different stenosis severities: 50% and 78% [17,35]. They analysed also the influence of pressure loads and stenosis severity on the cyclic compression of plaques [12,36].

The effect of plaque length has never been investigated in the literature. The present paper aims at addressing this lack. A FSI 2D axisymmetric model of the blood flow in a smooth pipe is considered, with a thick, deformable, heterogeneous and axisymmetric stenosis, mimicking an atherosclerotic plaque in a straight segment of artery. The model allows rapid modifications of the geometrical and constitutive parameters of the plaque for evaluating the influence of all these parameters.

## 2. Methods

### 2.1 Geometrical model

A schematic of the geometry in the reference configuration (i.e. in unloaded pressure-free conditions [32,37]) is provided in Fig. 1. The model of the plaque is axisymmetric (Fig. 1-D). The initial stenosis shape starts from a sinus shape function along the longitudinal direction. It is composed of the healthy arterial wall outside and of a fibrous cap containing the lipid core inside (Fig. 1-B).

The healthy arterial lumen has an inner radius of  $R_0 = 3\text{ mm}$  and a wall thickness of  $h_0 = 0.5\text{ mm}$  (Fig. 1-C), which corresponds to average values for the wall of the carotid artery [38].

Most of vulnerable carotid plaques present a positive remodelling [39] which is modelled as an external remodelling radius of the vessel. It is set here to  $R_m = 1\text{ mm}$  [39].

The reference for the plaque length is set to  $L=10\text{ mm}$ . This value corresponds to the average length of carotid plaques [40]. The stenosis height  $H_0$  is related to the stenosis severity, denoted  $S$ . Eq. 1 gives the expression of the stenosis severity as the ratio between the stenosis height and the healthy radius [5,6]. In the present study as in [5,6], the radius severity is considered. Clinicians sometimes consider the stenosis severity in terms of cross-sectional area reduction (denoted  $S_{area}$ ). Eq. 2 gives the conversion formula between the radius severity and the area severity.

$$S = 1 - \frac{R_0 - H_0 - e}{R_0} \quad (1)$$

$$S_{area} = 1 - (1 - S)^2 \quad (2)$$

203

204 According to NASCET or ECST studies [5,6], a plaque is vulnerable if the stenosis radius  
 205 severity is above 70%. However it is widely believed that this criterion alone is not sufficient  
 206 to characterize the vulnerability of plaques [1]. The current study considers moderately severe  
 207 plaques (reference value  $S=45\%$ ) and investigate the effect of other parameters on the  
 208 vulnerability.

209

210 The fibrous cap thickness is a critical geometrical characteristic for plaque vulnerability  
 211 because thrombo-embolic events result from the fibrous cap rupture. To place the study in a  
 212 case of vulnerable plaque, a thin fibrous cap is considered ( $e=0.1\text{mm}$ ) [15]. To simplify the  
 213 idealized plaque model, the fibrous cap thickness is homogeneous along the stenosis.

214

215 The arterial length upstream stenosis is set to 20 mm. This is necessary for establishing the  
 216 flow without having the influence of inflow boundary conditions prescribed at the inlet. For  
 217 the same reason, the arterial length downstream the stenosis is set to 50 mm ensuring the  
 218 establishment of the eventual flow recirculation.

219

## 220 **2.2 Fluid and structural equations**

221

222 A pulsatile flow of a viscous Newtonian and incompressible fluid is considered in an  
 223 axisymmetric pipe (Fig. 1-A), with a pulsation  $\omega = 2\pi$  [41]. This flow behaviour is suitable  
 224 for simulating the flow in large arteries because Non-newtonian effects are believed to have a



minor influence (see discussion in section 4.3). Its dynamic viscosity is denoted  $\eta_f$  and the density of the fluid is denoted  $\rho_f$ . The fluid velocity field  $\mathbf{v}_f$  and pressure field  $p$  are governed by the unsteady incompressible Navier-Stokes equations written in the Arbitrary Lagrangian-Eulerian (ALE) formulation [42]:

$$\begin{cases} \rho_f \frac{\partial \mathbf{v}_f}{\partial t} + \rho_f (\mathbf{v}_f - \mathbf{w}) \cdot \nabla \mathbf{v}_f - \nabla \cdot \boldsymbol{\sigma}_f = \mathbf{0} \\ \nabla \cdot \mathbf{v}_f = 0 \end{cases} \quad \text{in } \Omega_f, \quad (3)$$

where  $\mathbf{w}$  is the mesh velocity related to the ALE formulation,  $\boldsymbol{\sigma}_f$  the Cauchy stress tensor in the fluid and  $\Omega_f$  is the fluid domain depicted in Fig.1-A.

The displacement vector, denoted  $\mathbf{u}_s$ , and the Cauchy stress tensor, denoted  $\boldsymbol{\sigma}_s$ , of the solid part, with respect to the reference configuration, satisfy the following equation [43]:

$$\rho_s \frac{\partial^2 \mathbf{u}_s}{\partial t^2} - \nabla \cdot \boldsymbol{\sigma}_s = \mathbf{0} \quad \text{in } \Omega_s, \quad (4)$$

where  $\Omega_s$  is depicted in Fig.1-A and  $\rho_s$  is the density of the constituents in the solid domain, which is assumed homogeneous.

### 2.3 Fluid and structural boundary conditions

At the inlet of the fluid domain, a Womersley velocity profile [44] is applied and at the outlet, a pressure is imposed implying no normal viscous stress (see Eq. 5). The time variations of the pressure and the velocity profiles are written using Fourier decomposition, with 18 and 6 terms respectively for ensuring agreement with experimental data. Fourier decomposition is applied to the temporal signals shown in Fig. 2.

$$\begin{cases}
\mathbf{v}_f(r, t) = -\frac{c_0}{4\eta_f} R^2 \left(1 - \left(\frac{r}{R}\right)^2\right) - \frac{R^2}{\eta_f} \sum_{k=0}^6 \operatorname{Re} \left( \frac{ic_k}{\alpha_k^2} \left(1 - \frac{J_0(\alpha_k \frac{r}{R} i^{\frac{3}{2}})}{J_0(\alpha_k i^{\frac{3}{2}})}\right) e^{ik\omega t} \right) \mathbf{e}_z & \text{on } \partial^{in}\Omega_f \\
p(t) = \sum_{k=0}^{18} \operatorname{Re}(p_k e^{ik\omega t}) & \text{on } \partial^{out}\Omega_f \\
\boldsymbol{\sigma}_f^{viscous} \mathbf{e}_z = \mathbf{0} & \text{on } \partial^{out}\Omega_f
\end{cases}, \quad (5)$$

where  $\partial^{in}\Omega_f$  and  $\partial^{out}\Omega_f$  are respectively the inlet and the outlet boundaries of the fluid depicted in Fig. 1-A,  $\mathbf{e}_z$  is the longitudinal vector and  $J_0$  is the zero order Bessel function of first kind,  $R$  is the radius of the pipe at the inlet and  $(\alpha_k = R \sqrt{\frac{k\omega\rho_f}{\eta_f}})_{0 \leq k \leq 6}$  is the series of Womersley numbers.

$\sigma_f^{viscous}$  represents the viscous stress part of the Cauchy stress tensor in the fluid  $\sigma_f$  (see Eq. 8 in the section 2.4).

The axial velocity at the inlet is represented in Fig. 2-A and the pressure at the outlet is represented in Fig. 2-B [46].

The Fourier coefficients  $c_k$  (Tab. 3) of the Womersley profile are computed from the axial velocity data measured non-invasively using PC-MRI in the common carotid artery of a volunteer [46]. Moreover the pressure Fourier coefficients  $p_k$  (Tab. 3) are deduced from the variations over cardiac cycles of the pressure measured non-invasively using the applanation tonometry technique on the same volunteer [47].

At the boundaries of the elastic solid, the displacement vector  $\mathbf{u}_s$  and the Cauchy stress tensor  $\boldsymbol{\sigma}_s$ , with respect to the reference configuration, satisfy the following equations [43]:

$$\begin{cases} \boldsymbol{\sigma}_s \mathbf{n}_{s,ext} = \mathbf{0} & \text{on } \partial^{ext} \Omega_s \\ \mathbf{u}_s \cdot \mathbf{e}_z = 0 & \text{on } \partial^{in} \Omega_s \text{ and } \partial^{out} \Omega_s \end{cases}, \quad (6)$$

where  $\partial^{ext} \Omega_s$ ,  $\partial^{in} \Omega_s$ ,  $\partial^{out} \Omega_s$  and the normal vector  $\mathbf{n}_{s,ext}$  are depicted in Fig.1-A.

At the fluid-structure interface  $\partial \Omega_{fs}$  (see Fig. 1-A), the kinematic and dynamic conditions apply, ensuring continuity of velocity fields and normal stresses:

$$\begin{cases} \mathbf{v}_f = \frac{\partial \mathbf{u}_s}{\partial t} = \mathbf{w} \\ \boldsymbol{\sigma}_s \mathbf{n}_s + \boldsymbol{\sigma}_f \mathbf{n}_f = \mathbf{0} \end{cases} \text{ on } \partial \Omega_{fs}, \quad (7)$$

where  $\partial \Omega_{fs}$  and the normal vectors  $\mathbf{n}_f$  and  $\mathbf{n}_s$  are depicted in Fig. 1-A. In the fluid domain, mesh velocity  $\mathbf{w}$  is derived following a Laplace smoothing method from the interface conditions.

## 2.4 Fluid and structural properties

In a viscous Newtonian incompressible fluid, the expression of the Cauchy stress tensor depends linearly on the strain rate:

$$\boldsymbol{\sigma}_f = -p\mathbf{I} + \eta_f (\nabla \mathbf{v}_f + {}^t \nabla \mathbf{v}_f), \quad (8)$$

282 with  $\eta_f = 0.005 \text{ Pa.s}$  [42]. The first and second terms are respectively the hydrostatic  
 283 component  $\boldsymbol{\sigma}_f^{hydrostatic}$  and the viscous stress component  $\boldsymbol{\sigma}_f^{viscous}$ . The density of the fluid is set  
 284 to  $\rho_f = 1050 \text{ kg/m}^3$  [41].

285  
 286 Holzapfel et al. established a hyperelastic anisotropic constitutive equation for artery  
 287 components [48]. This model is used here for each component of the plaque. Hyperelasticity  
 288 implies the existence of a strain energy density function  $\varphi$  depending upon the Green-Cauchy  
 289 right strain tensor  $\mathbf{C} = {}^t\mathbf{F}\mathbf{F}$ , where  $\mathbf{F}$  is the deformation gradient tensor [43]. Thus  $\varphi = \varphi(\mathbf{C})$   
 290 and the associated Cauchy stress tensor is given by:

$$291 \quad \boldsymbol{\sigma}_s = 2J^{-1}\mathbf{F}\frac{\partial\varphi}{\partial\mathbf{C}}\mathbf{F}, \quad (9)$$

292 where  $J = \det(\mathbf{F})$  is the volume change invariant. This formulation is valid for a solid without  
 293 residual stresses. It was proposed in [48] to separate the isotropic and the anisotropic part of  
 294  $\varphi$ . The anisotropy is defined by two preferred directions corresponding to two families of

295 collagen fibres. The angle between these two families of fibres is denoted  $\beta$ .  $\mathbf{M} = \begin{pmatrix} 0 \\ \cos(\beta) \\ \sin(\beta) \end{pmatrix}$

296 and  $\mathbf{M}' = \begin{pmatrix} 0 \\ \cos(\beta) \\ -\sin(\beta) \end{pmatrix}$  represent the directions of fibres in the local coordinate system.

297  
 298 Then, the strain energy density  $\varphi$  is written such as:

$$299 \quad \varphi(I_1, I_4, I_6, J) = \frac{c}{2}(I_1 - 3) + \frac{k_1}{2k_2} \sum_{i=4,6} (e^{k_2(I_i-1)^2} - 1) + \frac{\kappa}{2}(J - 1)^2, \quad (10)$$

300 where  $I_1 = \text{tr}(\mathbf{C})$ ,  $I_4 = \mathbf{M} \cdot (\mathbf{C}\mathbf{M})$  and  $I_6 = \mathbf{M}' \cdot (\mathbf{C}\mathbf{M}')$ ,  $c$ ,  $\kappa$ ,  $k_1$  and  $k_2$  are material  
 301 parameters. Arterial tissue is often assumed as nearly incompressible [49]. The modulus of

compressibility  $\kappa$  is set to 500,000 kPa here in order to ensure this hypothesis. The density is set to  $\rho_s = 900 \text{ kg/m}^3$ . Reference values of parameters  $c$ ,  $k_1$  and  $k_2$  are given in Tab. 1. They were taken from experimental data [50].

To simplify the model, average properties of the media and of the adventitia reported in [50] are taken. For deducing the properties of the healthy artery reported in Tab. 1, a weighted average is derived, with a weight of  $\frac{2}{3}$  for the media and a weight of  $\frac{1}{3}$  for the adventitia [38]. The equation used to derive parameter  $c$  is given Eq. 11. A similar equation is used for the other mechanical parameters ( $k_1$ ,  $k_2$  and  $\beta$ ).

$$c^{wall} = \frac{2}{3}c^{media} + \frac{1}{3}c^{adventitia} \quad (11)$$

## 2.5 Numerical computation

FSI simulations are performed using commercial FE solver COMSOL Multiphysics [51]. The compatible finite-element types are  $P_2$  for the fluid velocity  $\mathbf{v}_f$ ,  $P_1$  for the fluid pressure  $p$  and  $P_2$  for the solid displacement  $\mathbf{u}_s$  [52]. The model geometry is meshed using triangular mesh generation in COMSOL Multiphysics, consisting in  $N_f$  elements for the fluid domain ( $2680 \leq N_f \leq 3316$ ) and  $N_s$  for the solid domain ( $3476 \leq N_s \leq 4325$ ), with  $N_{fibrous\ cap}$  elements in the thickness of the fibrous cap ( $1025 \leq N_{fibrous\ cap} \leq 1650$ ), depending on the different model geometries considered in the parametric study. The coupled fluid-structure problem is discretized using a Galerkin-Least-Square method (GLS) and an implicit temporal discretization of order 5 using a Backward Differentiation Formula (BDF) with an adaptive time step. The non-linear problems are solved using a Newton-Raphson algorithm.

The mesh is refined close to the wall in order to take into account the viscous boundary layer: the mesh size is prescribed 3 times finer near the wall than at the centre.

The minimum and the maximum Reynolds number (Eq. 12) are respectively  $Re_{min}=300$  and  $Re_{max}=2000$ . The value of  $Re_{max}$  justifies the use of a turbulence model [41]. The flow is modelled as being turbulent with the  $k-\omega$  model [51].

$$Re = \frac{\rho V D}{\mu}, \quad (12)$$

where  $D$  is the inner diameter of the artery and  $V$  is the axial velocity: for  $Re_{min}$ ,  $D$  and  $V$  are taken at diastole in the healthy artery upstream the plaque and for  $Re_{max}$ ,  $D$  and  $V$  are taken at systole at the top of the stenosis.

The geometry described in section 2.1 is the unloaded pressure-free geometry corresponding to the initial condition of the numerical computation. The simulation is performed over four cardiac cycles. During the first cardiac cycle, the pressurization and the average blood flow are applied before considering pulsatile effects. During this stage, the fluid viscosity, the pressure at the outlet and the velocity at the inlet are set gradually in order to ensure numerical convergence:

- the axial velocity at the inlet is increased linearly from 0m/s to 0.3m/s (see  $v_z(t=0)$  Fig. 2-A)
- the pressure at the outlet is increased linearly from 0mmHg to 91mmHg (see  $p(t=0)$  Fig. 2-B)
- the fluid viscosity is decreased linearly from 0.05Pa.s to 0.005Pa.s

Afterwards, three cycles of the actual pulsatile flow (see Fig. 2) are computed. The flow is fully established and periodic over the last cycle. Hence, the last cycle is used for the analysis.

## 2.6 Parametric study

In our model, different plaque parameters are set for reproducing the variability of real plaques:

- the fibrous cap thickness denoted  $e$ ,
- material parameter  $k_1$  in the arterial wall and in the fibrous cap, respectively denoted  $k_1^{wall}$  and  $k_1^{cap}$ ,
- stenosis severity  $S$  defined in Eq. 1
- stenosis length  $L$ .

Each parameter is set independently of the other parameters (unidirectional parametric study).

The geometrical properties of the reference model are:  $e = 0.1$  mm,  $S = 45\%$ ,  $L = 10$  mm. The reference values for  $k_1$  are reported in Tab. 1. Simulations and analysis are performed for a wide range of these parameters using an interface between the COMSOL software and the MATLAB software [51,53].

The current study considers moderately severe plaques, between 20% and 70%. The current study is more focused on the effect of the stenosis length, as the effect of this parameter is not clearly understood and there exists a large range of plaque lengths. Plaques in the carotid artery may be short ( $L < 10$  mm) [18,40]. Therefore, plaque lengths ranging between 5 mm and 20 mm are considered in this study (20 mm corresponds to a very long plaque [40]).

The fibrous cap thickness and the material parameters are taken into account for investigating the effect of the plaque stiffness.

## 2.7 Analysed criteria

The analysis is focused on the response at the systole. A special attention is paid to the four following criteria:

- the maximum von Mises equivalent stress in the fibrous cap defined as,

$$\sigma_{\max}^{VM} = \text{Max}(\sigma^{VM}) = \text{Max}(\sqrt{\sigma_1^2 + \sigma_2^2 - \sigma_1\sigma_2}), \quad (13)$$

where  $\sigma_1$  and  $\sigma_2$  are the principal stresses in the radial and longitudinal directions

- the maximum wall shear stress (WSS),

$$\tau_{\max} = \text{Max}(\|\boldsymbol{\sigma}_f^{\text{viscous}} \mathbf{n}_f\|) \quad (14)$$

- the average radial strain of the plaque,

$$\varepsilon_R = \frac{U_R}{H_0 + h_0 + e + R_m}, \quad (14)$$

where  $U_R$  is the radial displacement of the fibrous cap at the middle of the stenosis,

- the global shear strain of the plaque,

$$\gamma = \frac{U_z}{H_0 + h_0 + e + R_m}, \quad (16)$$

where  $U_z$  is the longitudinal displacement of the fibrous cap at the middle of the stenosis.



The maximum von Mises equivalent stress,  $\sigma_{\max}^{VM}$ , defined in Eq. 13, is chosen to reflect the vulnerability of the plaque. The maximum WSS,  $\tau_{\max}$ , is mostly associated with the formation, growth and remodelling of the plaque [19-21,54].

Criteria  $\gamma$  and  $\varepsilon_R$  give an indication about the deformability of the plaque. The larger  $\gamma$ , the more deformable the plaque by shear. This mode of deformation is mostly induced by the drag force of the flow. The larger  $\varepsilon_R$ , the more deformable the plaque in compression. This mode of deformation is mostly induced by the pressure variations.

## 2.8 Convergence study

The four criteria presented in section 2.7 are used for assessing the convergence of the numerical resolution.

Temporal convergence is obtained using an adaptative time step, with a maximal value of 0.001s. It was checked that the four criteria remain unchanged by decreasing the maximum value of the time step.

The spatial convergence is obtained using over 2680  $P_2P_1$  elements for the fluid domain and over 3476  $P_2$  elements for the solid domain. It has been checked that increasing the degree of the shape functions to  $P_3$  for the fluid velocity,  $P_2$  for the fluid pressure and  $P_3$  for the solid displacement has only a marginal influence on the analysed criteria (Tab. 2).

### 3. Results

#### 3.1. Response of the stenosed artery

An example of results obtained from a FE analysis is shown in Fig. 3. Fig. 3-A shows the distribution of the von Mises equivalent stress in the plaque and in the healthy artery upstream and downstream the plaque, using a colour-coded representation plotted onto the deformed geometry at the systole. For visualizing the deformation between diastole and systole, the shape of the stenosed artery at diastole is represented in grey.

The percentage of diameter change between diastole and systole is about 5% in the healthy part of the artery (Fig. 3-A2), which corresponds to physiological conditions measured using MRI [46]. The percentage of diameter change is smaller in the stenosed region, due to the stiffening effect of the wall thickening (Fig. 3-A2).

The longitudinal component of the velocity  $v_z = \mathbf{v}_f \cdot \mathbf{e}_z$  is also represented at systole in Fig. 3-B using a colour-coded representation. Due to Venturi effect, the velocity increases from about 0.5m/s upstream the stenosis to about 1.7m/s downstream the stenosis. Recirculation occurs downstream the stenosis.

In the next sections, the results of the parametric study are presented. In Fig. 4 and 5, the influence of parameters  $e$ ,  $k_1^{wall}$  and  $k_1^{cap}$ ,  $S$ ,  $L$ , onto  $\sigma_{\max}^{VM}$ ,  $\tau_{\max}$ ,  $\varepsilon_R$  and  $\gamma$  is displayed.

#### 3.2. Influence of the fibrous cap thickness.

The influence of the fibrous cap thickness  $e$  onto the mechanical criteria is studied. For that, parameters  $(S,L)$  are set to (45%,10mm) and  $k_1^{wall}$  and  $k_1^{cap}$  are set to the values reported in Tab. 1. The increase of  $\sigma_{max}^{VM}$  with respect to the decrease of the fibrous cap thickness  $e$ , shown in Fig. 4-A1, is in agreement with other studies stating that a thin fibrous cap is the parameter mostly associated with the plaque vulnerability [15,23]. The increase of  $\sigma_{max}^{VM}$  is more important from  $e=0.1\text{mm}$  to  $e=0.05\text{mm}$ . This result can be related to the result of Li et al. [15]. They showed that  $e \leq 0.1\text{mm}$  could result in plaque rupture, even for a small stenosis severity.

The ratio between the volume of the lipid core and the fibrous cap thickness is sometimes used to characterise the plaque vulnerability: the greater this ratio, the more vulnerable the plaque [55] but Gao and Long [27] showed that the stress level in the fibrous cap is more sensitive to the fibrous cap thickness than to the lipid core volume.

Moreover as shown in Fig. 4, when  $e$  decreases, the average compression strain  $\varepsilon_R$  decreases, whereas the average shear strain  $\gamma$  and the maximal WSS  $\tau_{max}$  increases.

The stress criteria  $\sigma_{max}^{VM}$  and  $\tau_{max}$  and the deformation criteria  $\varepsilon_R$  and  $\gamma$  will be analysed in the discussion considering a thin and homogenous fibrous cap ( $e=0.1\text{mm}$ ).

### 3.3 Influence of the stiffness of the constituents.

The influence of the material parameters  $k_1^{wall}$  and  $k_1^{cap}$  onto the mechanical criteria are studied considering that the other parameters are set to  $(e,S,L)=(0.1\text{mm},45\%,10\text{mm})$ . These

parameters are increased in the following range of values (in kPa):  $24.53 \leq k_1^{wall} \leq 300$  and  $23.7 \leq k_1^{cap} \leq 300$ .

The variations of  $\sigma_{max}^{VM}$  with respect to  $k_1^{wall}$  and  $k_1^{cap}$  (Fig. 4-A2,A3) shows that the plaque is more stable when each of these parameters increases. This result is in agreement with other studies reporting that a calcified plaque (stiffer) is more stable. Moreover Imoto et al [56] showed that a calcified inclusion in the fibrous cap can stabilize the plaque. However, Vengrenyuk et al. [57] showed that a fibrous cap with micro-calcification inclusions is related with high stress concentration and plaque fracture. This means that local and small inclusions may have the opposite effect of large calcifications.

The effect of  $k_1^{wall}$  and  $k_1^{cap}$  on the other parameters (compression strain  $\varepsilon_R$  and average shear strain  $\gamma$ ) is marginal within the range of tested values. Moreover, the mechanical properties of the healthy part of the artery affect only slightly the maximal WSS  $\tau_{max}$ , whereas the mechanical properties of the fibre cap on the WSS is more pronounced. The decrease of  $\tau_{max}$  with regard to an increase of  $k_1^{cap}$  is interesting; it shows that a compliant plaque is more prone to local erosion by wall shear stress. The behaviour of a compliant plaque, using the material parameters given in Tab. 1 [50], onto the stress and deformation criteria will be detailed in the discussion.

### 3.4 Influence of the stenosis severity

The effects of the stenosis severity is investigated through the following range of values:  $25\% < S < 70\%$  with a constant plaque length  $L=10\text{mm}$ . The fibrous cap thickness is set to  $e=0.1\text{mm}$  and the values of  $k_1^{wall}$  and  $k_1^{cap}$  are reported in Tab. 1. In current clinical practice,

when a vulnerable plaque is subjected to triggering events, the degree of severity of endoluminal stenosis (Eq. 1) is evaluated and the plaque is diagnosed as vulnerable if this criterion is beyond 70% [5,6]. With our model, the mechanical response is analyzed within a range of stenosis severities which are below the vulnerability threshold. Fig. 5-A (left) shows that  $\sigma_{\max}^{VM}$  is around 400kPa for  $20\% \leq S \leq 45\%$  ( $\sigma_{\max}^{VM}(20\%) = 404.53$  kPa,  $\sigma_{\max}^{VM}(35\%) = 413.19$  kPa and  $\sigma_{\max}^{VM}(45\%) = 384.46$  kPa) and increases to around 500kPa for  $S=55\%$  ( $\sigma_{\max}^{VM}(55\%) = 540.31$  kPa) and to around 600kPa for  $S=70\%$  ( $\sigma_{\max}^{VM}(70\%) = 627.80$  kPa) which confirms that the degree of endoluminal stenosis affects the plaque vulnerability.

### 3.5 Influence of the stenosis length

Moreover, Fig. 5-A (right) shows that the plaque length is also strongly related to the plaque vulnerability even though this criterion is not taken into account in clinical practice. For instance, on one hand, the plaque with the parameters  $(S,L)=(55\%,10\text{mm})$  has a similar  $\sigma_{\max}^{VM}$  value as the plaque with the parameters  $(S,L)=(45\%,5\text{mm})$ :  $\sigma_{\max}^{VM}(55\%,10\text{mm})=540.31$  kPa and  $\sigma_{\max}^{VM}(45\%,5\text{mm})=541.21$  kPa. On the other hand, for two plaques having the same severity  $S=45\%$ , the maximum stress  $\sigma_{\max}^{VM}$  is 50% larger in the short plaque ( $L=5\text{mm}$ ) than in a larger plaque ( $L=10\text{mm}$ ), and the maximum WSS  $\tau_{\max}$  is increased of 100%.

In Fig. 5, it can be remarked that increasing the stenosis severity or decreasing the plaque length has similar effects on the mechanical criteria. The influence of both the stenosis severity and the plaque length on the fluid structure interaction and on the plaque vulnerability will be discussed in the next section.

## 4. Discussion

### 4.1 Compression or shear effects

In Fig. 5-C and D, the deformability of the plaque is investigated through its average compression strain  $\varepsilon_R$  and its average shear strain  $\gamma$ . Considering that the stenosis length is set to  $L = 10\text{mm}$ , in Fig. 5-C and D (left), it can be noted that the mode of deformation changes drastically between  $S = 35\%$  and  $S = 45\%$ , inducing a transition. On one hand, below the transition, the compression strains overwhelm the shear strains. On the other hand, beyond the transition severity, the opposite effect occurs.

Increasing the stenosis severity or decreasing the plaque length has similar effects on the mechanical criteria. Considering that the stenosis severity is set to  $S = 45\%$ , in Fig. 5-C and D (right) it appears a transition zone between  $L = 10\text{mm}$  and  $L = 15\text{mm}$ . Beyond the transition length, the compression strains overwhelm the shear strains, whereas the opposite effect occurs for short stenoses.

This transition is illustrated in Fig. 6-A which shows the stress distribution in the fibrous cap ( $\sigma^{VM}$ ) for different severities and different lengths. It is noticeable that for  $(S, L) = (35\%, 10\text{mm})$  or for  $(S, L) = (45\%, 15\text{mm})$  the stress distribution is controlled by the blood pressure. In this case, high stresses are localized on the top of the stenosis. On the other hand, for  $(S, L) = (45\%, 10\text{mm})$  or for  $(S, L) = (55\%, 10\text{mm})$  or for  $(S, L) = (45\%, 5\text{mm})$ , the stress distribution is controlled shear which induces a localization of high stresses upstream stenosis.

If shear overwhelms compression, the plaque length has a significant effect onto the plaque vulnerability. The shorter the plaque, the more vulnerable.

If compression overwhelms shear, the study shows that a solid model without FSI, just considering pressure loads, is sufficient [23-26]. However, a model with FSI is necessary when the shear effects become significant [9,10,18,27-33]. This remark is interesting for choosing appropriate patient-specific models.

## **4.2 Plaque pinching**

If shear overwhelms compression, results shown in Fig. 6-A give an interesting explanation for the deformed shape of the fibrous cap. Indeed, it can be observed that the plaque is compressed from both sides of the stenosis, upstream and downstream, resulting in a pinching effect of the plaque. The pinching effect comes from the coupled action of two phenomena:

- the shear coming from two flows:
  - the global flow upstream stenosis
  - the flow recirculation downstream stenosis
- the depression coming from:
  - the Venturi effect on the top of the stenosis
  - the recirculation downstream stenosis

Each flow compresses the stenosis on both sides, upstream and downstream. This phenomenon is schematized in Fig. 7-A. Due to the Venturi effect and flow recirculation, the pressure decreases [58], inducing outward tractions onto the plaque. These phenomena may also induce buckling in the fibrous cap.

562

563 In Fig. 7-B, the response of the plaque has been plotted by considering only the action of the  
564 blood pressure, without the action of blood flow. The results show that the mechanical  
565 response is completely different, without pinching effect.

566

567 The pinching effect appears for moderately thin fibrous cap ( $e=0.2\text{mm}$ ) and increases when  
568 the fibrous cap thickness decreases. It is illustrated by the increase of the shear strain  $\gamma$  and the  
569 decrease of the compression strain  $\varepsilon_R$  with respect to the decrease of the fibrous cap thickness  
570  $e$ , respectively shown in Fig. 4-C1 and D1.

571

572 As shown in Fig. 6-A, the plaque pinching does not present an upstream-downstream  
573 symmetry. For instance, for  $L=5\text{mm}$  and for  $S=55\%$  (Fig. 6-A), there is no symmetry because  
574 the global flow, the flow recirculation and the recirculation depression do not produce the  
575 same magnitude of force acting upstream and downstream the stenosis.

576

577 This puts in evidence that the action of blood flow is essential because it induces stress  
578 concentrations. Tang et al. evoked already that a local stress concentration is more closely  
579 related to plaque fracture [9] but the pinching effect has never been referenced.

580

581 Localization of the WSS ( $\tau$ ) is also shown in Fig. 6-B, with high concentrations when the  
582 plaque is pinched. As WSS may be related with the plaque ulceration [19-21], the results  
583 show that when the pinching effect is strong, this may also induce plaque ulceration in real  
584 cases.

585

586 **4.3 Main limitations**



587

588 **The mechanical properties of the artery.** The Holzapfel material model was chosen because  
589 it is an appropriate model taking into account the nonlinear and anisotropic behaviour of  
590 arteries. Other material models could be used as Mooney-Rivlin models [28,59] and Ogden  
591 hyper-elastic models [13,15]. It has been verified that the pinching effect and the importance  
592 of plaque length are preserved even if these other material models are used. They are also  
593 preserved if different properties are considered for both layers of the healthy artery (media  
594 and adventitia, see section 2.4). Actually, as shown in Fig. 4-A2, B2, C2 and D2, the material  
595 properties of the healthy artery wall have a marginal influence on the pinching effect.

596 An important question is also the convexity of strain energy function defined in Eq. 10. As  
597 recommended by Holzapfel et al. [64], if  $I_4$  and/or  $I_6$  are less than 1, their contribution is  
598 cancelled from the strain energy function. This guarantees the convexity of the strain energy  
599 function whatever the material parameters.

600 Another important question is the impact of the choice of the material parameters of the artery  
601 on the mechanical response. The results displayed in Fig. 4 tend to show that the impact of the  
602 material properties of the artery onto the response of the plaque is less important than the  
603 impact of geometrical parameters like the severity, the thickness and the length.

604 However, the material properties of the artery used in the parametric study are defined as  
605 averages of the properties of the media and of the adventitia. It has been verified that this  
606 simplification does not alter the form of the mechanical response of the artery. For this  
607 verification, the longitudinal and circumferential stress/stretch curves of the different models  
608 of artery used in this paper have been plotted in Fig. 8 and compared to the stress/stretch  
609 curves of the original models taken from Gasser et al. [50]. It can be observed that the variety  
610 of parameters tested in our parametric study encompass the stress/stretch curves of the media  
611 and adventitia models reported in [50]. Moreover, the different curves have similar shapes,

which show that varying the parameters of the model results mainly in variations of the compliance of the artery itself.

**The perivascular tissues.** The vessel receives perivascular constraint from the surrounding tissues [60]. Considering the stiffness of the surrounding tissue may increase the rigidity of the structure, similarly as playing with the stiffness of the artery wall itself. It has been observed that the material properties of the healthy artery wall have a marginal influence on the analysed mechanical criteria (Fig. 4-A2, B2, C2 and D2). Then the effect of the surrounding tissue may not be considered as prominent.

**The blood viscosity.** Stenoses have an influence on the blood flow but can also have an impact on its viscosity. The blood is not a Newtonian fluid. The blood, composed of 80% plasma, may be assumed as a Newtonian fluid in healthy arteries with diameter larger than 5 mm. But the presence of red cells influences the blood viscosity when the hematocrite (ratio between the volume of red cells and the volume of plasma) increases. It is the case when the arterial lumen decreases or when the red cells aggregates [41,61]. This aggregation occurs in an area with many red cells and where the shear stress is less than 1 Pa [62]. Such a zone can be localized in a recirculation like downstream the stenosis. The red cells are trapped in a zone where they can aggregate. This case should be taken into account if one would like to refine the local shear stress just downstream the stenosis.

**The boundary conditions.** The effect of pressure and flow variability is not analysed. Such analysis may be interesting with regard to the pinching effect and it will be achieved in the future. Moreover, the existence of an axial pretension in the artery (tethering effect) is also an

aspect that may be important, especially concerning the zero-stress state in real geometries [32,63]. Given that our geometries were ideal, this aspect was not considered.

**The geometry.** This study offers an analysis of the influence of plaque shape on fluid structure interactions especially concerning the plaque length. Nevertheless there is no axisymmetric plaque in real case and the dimensions of the plaque used in our study are not representative of a given physiological scenario. The dimensions of the plaque were defined for encompassing a wide range of possible scenarii regarding plaque lengths, plaque severities, fibre cap thickness and material properties of the tissues. Other models are under development: asymmetric plaques, axisymmetric plaques with shape irregularities. The radius of the artery used in this study is based on the dimensions of the human common carotid artery [43,65]. It would also be interesting to evaluate the effect of the artery radius for mimicking for instance the plaque behaviour in the internal carotid artery which is smaller.

#### **The unloaded state of the artery**

The arterial radius for the unloaded (no pressure) condition was set at 3.00 mm and the average arterial radius for the pressurized condition (Fig. 3-A2) was 3.625 mm at diastole and 3.825 mm at systole. This indicates an expansion of artery. This expansion was not calibrated upon physiological data. It was applied because the hyperelastic constitutive equations are a model of the mechanical behaviour with regard to the unloaded (no pressure) state of the artery. However, we did not study how the choice of the unloaded geometry affects the mechanical response of the plaque. Moreover, the effect of the axial prestretch is also an aspect that still has to be evaluated.

## 5. Conclusion

This study shows that geometric and mechanical properties of atheromatous plaques affect significantly its mechanical response to the action of pulsatile blood flow. Notably for a short, severe and compliant stenosis, the blood pinches the plaque. In this case the stress localization and plaque vulnerability is emphasized.

These results may offer some new perspectives for understanding the vulnerability of short plaques. Unfortunately there are only few experimental papers available on this subject in the literature. Future work will consist in achieving such experimental investigations for characterizing the vulnerability of short plaques from clinical data. Moreover, more sophisticated models are under development in order to evaluate the effects of shape irregularities and asymmetry.

677 **6. Conflict of interest**

678

679 None.

680

681 **7. Acknowledgements**

682

683 This study is part of the Imandef project (Grant ANR-08-JCJC-0071) funded by the ANR  
684 (French National Research Agency).

685

## References

- [1] Rosamond W, Flegal K et al.. Heart Disease and Stroke Statistics - 2007 Update. A Report From the American Heart Association Statistics Committee and Stroke Statistics Subcommittee. *Circulation* 2007;115:69-171.
- [2] Virmani R, Ladich E, Burke A, Kolodgie F. Histopathology of Carotid Atherosclerotic Disease. *Neurosurgery* 2006;59(5):219-227.
- [3] Lipinsky MJ, Frias JC, Fayad HA. Advances in detection and characterization of atherosclerosis using contrast agent targeting the macrophage. *Journal of Nuclear Cardiology* 2006;13:699-609.
- [4] Carr S, Farb A, Pearce WH, Virmani R, Yao JST. Atherosclerotic plaque rupture in symptomatic carotid artery stenosis. *Journal of Vascular Surgery* 1996;23:755-766.
- [5] ECST, MRC European Carotid Surgery Trial. Interim results for symptomatic patients with severe (70%-99%) or with mild (0%-29%) carotid stenosis. European Carotid Surgery Trialists Collaborative Group. *The Lancet* 1991;337:1235-1243.
- [6] NASCET. Beneficial effect of carotid endarterectomy in symptomatic patients with high grade stenosis. *The New England Journal of Medicine* 1991;325:445-453.
- [7] Toussaint JF, LaMuraglia GM, Southern JF, Fuster V, Kantor HL. MR images of lipid, fibrous, calcified, hemorrhagic and thrombotic components of human atherosclerosis in vivo. *Circulation* 1996;94:932-938.
- [8] Cai JM, Hatsukami TS, Ferguson MS, Small R, Polissar NL, Yuan C. Classification of human carotid atherosclerotic lesions with in vivo multicontrast magnetic resonance imaging. *Circulation* 2002;106:1368-1373.
- [9] Tang D, Yang C, Zeng J, Woodard PK, Saffitz JE, Petrucci JD, Sicard GA, Yuan C. Local Maximal Stress Hypothesis and Computational Plaque Vulnerability Index for

710       Atherosclerotic Plaque Assessment. *Annals of Biomedical Engineering* 2005;33:1789–  
711       1801.

712 [10] Tang D, Teng Z, Canton G, Yang C, Ferguson M, Huang X, Zheng J, Woodard PK,  
713       Yuan C. Sites of Rupture in Human Atherosclerotic Carotid Plaques Are Associated  
714       With High Structural Stresses. An In Vivo MRI-Based 3D Fluid-Structure Interaction  
715       Study. *Stroke* 2009;40:3258-3263.

716 [11] Bank AJ, Versluis A, Dodge SM, Douglas WH. Atherosclerotic plaque rupture: a fatigue  
717       process. *Medical Hypotheses* 2000;55(6):480-484.

718 [12] Tang D, Yang C, Walker H, Kobayashi S, Ku DN. Simulating cyclic artery compression  
719       using a 3D unsteady model with fluid-structure interactions. *Computers and structures*  
720       2002;80:1651-1665.

721 [13] Versluis A, Bank AJ, Douglas WH. Fatigue and plaque rupture in myocardial infarction.  
722       *Journal of Biomechanics* 2006;39:339-347.

723 [14] Ohayon J, Finet G, Gharib AM, Herzka DA, Tracqui P, Heroux J, Rioufol G, Kotys MS,  
724       Elagha A, Pettigrew RI. Necrotic core thickness and positive arterial remodeling index:  
725       emergent biomechanical factors for evaluating the risk of plaque rupture. *American*  
726       *Journal of Physiology – Heart and Circulatory Physiology* 2008;295:717-727.

727 [15] Li ZY, Howarth SPS, Tang T, Gillard JH. How critical is fibrous cap thickness to carotid  
728       plaque stability? A flow-plaque interaction model. Simulation of the interaction between  
729       blood flow and atherosclerotic plaque. *Stroke* 2006;37:1195-1199.

730 [16] Li MX, Beech-Brandt JJ, John LR, Hoskins PR, Easson WJ. Numerical Analysis of  
731       pulsatile blood flow and vessel wall mechanics in different degrees of stenoses. *Journal*  
732       *of Biomechanics* 2007;40:3715-3724.

- [17] Tang D, Yang C, Ku DN. A 3-D thin wall model with fluid-structure interactions for blood flow in carotid arteries with symmetric and asymmetric stenoses. *Computers and structures* 1999;72:357-377.
- [18] Tang D, Woodard PK, Zeng J, Huang X, Yang C, Ferguson M, Yuan C, Canton G, Teng Z. 3D Critical Plaque Wall Stress Is a Better Predictor of Carotid Plaque Rupture Sites Than Flow Shear Stress: An In Vivo MRI-Based 3D FSI Study. *Journal of Biomechanical Engineering* 2010;132:031007-1-9.
- [19] Groen HC, Gilsen FJH, van der Lugt A, Ferguson MS, Hatsukami TS, van der Stenn AFW, Yuan C, Wentzel JJ. Plaque fracture in carotid artery is localized at the high shear stress region: A case report. *Stroke* 2007;38:2379-2381.
- [20] Cheng C, Tempel D, van Haperen R, van der Baan A, Grosveld F, Daemen MJAP, Krams R, de Crom R. Atherosclerotic lesion size and vulnerability are determined by patterns of fluid shear stress. *Circulation* 2006;113:2744-2753.
- [21] Fukumoto Y, Hiro T, Yamada J, Okamura T, Matsuzaki M. Localized elevation of shear stress is related to coronary plaque rupture: a 3-dimensional intravascular ultrasound study with in vivo color mapping of shear stress distribution. *Journal of American College of Cardiology* 2008;51(6):645-650.
- [22] Richardson PD, Davies MJ, Born GVR. Influence of plaque configuration and stress distribution on fissuring coronary atherosclerotic plaques. *The Lancet* 1989;334:941-944.
- [23] Loree HM, Kamm RD, Stringfellow RG, Lee RT. Effects of Fibrous Cap Thickness on Peak Circumferential Stress in Model Atherosclerotic Vessels. *Circulation Research* 1992;71:850-858.



- [24] Ohayon J, Teppaz P, Finet G, Rioufol G. *In vivo* prediction of human coronary plaque rupture location using intravascular ultrasound and the finite element method. *Coronary Artery Disease* 2001;12:655-663.
- [25] Ohayon J, Finet G, Treyve F, Rioufol G, Dubreuil O. A three-dimensional finite element analysis of stress distribution in a coronary atherosclerotic plaque: *In-vivo* location of plaque rupture location. *Biomechanics applied to Computer Assisted Surgery* 2005:225-241.
- [26] Li ZY, Howarth S, Trivedi R, Kim-Im JMU, Graves MJ, Brown A, Wang L, Gillard JH. Stress analysis of carotid plaque fracture based on in vivo high resolution MRI. *Journal of Biomechanics* 2006;39:2611-2622.
- [27] Gao H, Long Q. Effects of varied lipid core volume and fibrous cap thickness on stress distribution in carotid arterial plaques. *Journal of Biomechanics* 2008;41:3053–3059.
- [28] Tang D, Yang C, Zheng J, Woodard PK, Sicard GA, Saffitz JE, Yuan C. 3D MRI-Based Multicomponent FSI Models for Atherosclerotic Plaques. *Annals of Biomedical Engineering* 2004;32(7):947-960.
- [29] Yang C, Tang D, Yuan C, Hatsukami TS, Zheng J, Woodard PK. In Vivo/Ex Vivo MRI-based 3D Non-Newtonian FSI Models for Human Atherosclerotic Plaques Compared with Fluid/Wall-Only Models. *National Institutes of Health Public Access* 2007;19(3):233-246.
- [30] Kock SA, Nygaard JV, Eldrup N, Fründ ET, Klaerke A, Paaske WP, Falk E, Yong Kim W. Mechanical stresses in carotid plaques using MRI-based fluid–structure interaction models. *Journal of Biomechanics* 2008;41:1651-1658.
- [31] Leach JR, Rayz VL, Soares B, Wintermark M, Mofrad M, Saloner D. *Annals of Biomedical Engineering* 2010;38(8):2748-2765.

- [32] Huang X, Yang C, Yuan C, Liu F, Canton G, Zheng J, Woodard PK, Sicard GA, Tang D. Patient-specific artery shrinkage and 3D zero-stress state in multi-component 3D FSI models for carotid atherosclerotic plaques based on in vivo MRI data. *Molecular and Cellular Biomechanics*. 2009Jun;6(2):121-34.
- [33] Gao H, Long Q, Das KS, Halls J, Graves M, Gillard JH, Li ZY. Study of carotid arterial plaque stress for symptomatic and asymptomatic patients. *Journal of Biomechanics* 2011;44:2551-2557.
- [34] Valencia A, Baeza F. Numerical simulation of fluid-structure interaction in stenotic arteries considering two layer nonlinear anisotropic structural model. *International Communications in Heat and Mass Transfer* 2009;36:137-142.
- [35] Tang D, Yang C, Huang Y, Ku DN. Wall stress and strain analysis using a three-dimensional thick wall model with fluid structure interactions for blood flow in carotid arteries with stenoses. *Computers and structures* 1999;72:341-356.
- [36] Tang D, Yang C, Kobayashi S, Zheng J, Vito RP. Effect of Stenosis Asymmetry on Blood Flow and Artery Compression: A Three-Dimensional Fluid-Structure Interaction Model. *Annals of Biomedical Engineering* 2003;31:1182-1193.
- [37] Konala BC, Das A, Banerjee RK. Influence of arterial wall compliance on the pressure drop across coronary artery stenoses under hyperemic flow condition. *Mol Cell Biomech*. 2011; 8(1):1-20.
- [38] Fung YC. *Biomechanics: Mechanical Properties of Living Tissues*. Second Edition. Springer-Verlag NY Inc.. 1993.
- [39] Miura T, Matsukawa N, Sakurai K, Katano H, Ueki Y, Okita K, Yamada K, Ojika K. Plaque Vulnerability in Internal Carotid Arteries with Positive Remodeling. *Cerebrovascular Diseases Extra* 2011;1:54-65.

804 [40] Douglas AF, Christopher S, Amankulor N, Din R, Poullis M, Amin-Hanjani S,  
805 Ghogawala Z. Extracranial Carotid Plaque Length and Parent Vessel Diameter  
806 Significantly Affect Baseline Ipsilateral Intracranial Blood Flow. *Neurosurgery*  
807 2011Oct;69(4):767-73.

808 [41] Fung YC. *Biomechanics, Circulation*. Second Edition. Springer-Verlag NY Inc.. 1996.

809 [42] Formaggia L, Quarteroni A, Veneziani A. *Cardiovascular Mathematics, Modelling and*  
810 *Simulation of the circulatory system*. Volume 1. Springer. 2009.

811 [43] Fung YC, Tang P. *Classical and computational solid mechanics*. Volume 1. World  
812 Scientific. 2001.

813 [44] Uchida S. The Pulsating Viscous Flow Superposed on the Steady Laminar Motion of  
814 Incompressible Fluid in a Circular Pipe. *ZAMP* 1956;7(5):403-422.

815 [45] He X, Ku DN, Moore JE. Simple calculation of the velocity profiles for pulsatile flow in  
816 a blood vessel using Mathematica. *Annals of Biomedical Engineering* 1993;21(1):45-  
817 49.

818 [46] Avril S, Huntley JM, Cusack R. In vivo measurements of blood viscosity and wall  
819 stiffness in the carotid using PC-MRI. *European Journal of computational Mechanics*  
820 2009;18:9-20.

821 [47] Masson I, Boutouyrie P, Laurent S, Humphrey JD, Zidi M. Characterization of arterial  
822 wall mechanical behavior and stresses from human clinical data. *Journal of*  
823 *Biomechanics* 2008;41:2618–2627.

824 [48] Holzapfel GA, Gasser TC. A New Constitutive Framework for Arterial Wall Mechanics  
825 and a Comparative Study of Material Models. *Journal of Elasticity* 2000;61:1-48.

826 [49] Carew TE, Vaishnav RN, Patel DJ. Compressibility of the arterial wall. *Circulation*  
827 *Research* 1968;23:63-68.

828 [50] Gasser TC, Holzapfel GA. Modelling Plaque Fissuring and Dissection during Balloon  
829 Angioplasty Intervention. *Annals of Biomedical Engineering* 2007;35(5):711-723.

830 [51] COMSOL MULTIPHYSICS 3.4: Fluid-Structure Interaction Module. COMSOL-AB,  
831 Stockholm, Sweden.

832 [52] Zienkiewicz OC, Taylor RL. The Finite Element Method. Fifth Edition. Butterworth  
833 Heineman. 2002.

834 [53] MATLAB R2007a. The MathWorks Inc, Natick, USA.

835 [54] Yang C, Canton G, Yuan C, Ferguson M, Hatsukami TS, Tang D. Advanced human  
836 carotid plaque progression correlates positively with flow shear stress using follow-up  
837 scan data: An in-vivo MRI multi-patient 3D FSI study. *Journal of Biomechanics*  
838 2010;43(13):2530-2538.

839 [55] Oppenheim C, Touzé E, Leclerc X, Schmitt E, Bonneville F, Vandermarcq P, Gerardin  
840 E, Toussaint JF, Mas JL, Méder JF. IRM Haute résolution de l'athérosclérose  
841 carotidienne: au-delà de la lumière artérielle. *Journal de radiology* 2008;89 :293-301.

842 [56] Imoto K, Hiro T, Fujii T, Murashige A, Fukumoto Y, Hashimoto G, Okamura T,  
843 Yamada J, Mori K, Matsuzaki M. Longitudinal Structural Determinants of  
844 Atherosclerotic Plaque Vulnerability. *Journal of the American College of Cardiology*  
845 2005;46:735-1097.

846 [57] Vengrenyuk Y, Calier S, Xanthos S, Cardoso L, Ganaotos P, Virmani R, Einav S,  
847 Gilchrist L, Weinbaum S. A Hypothesis of Vulnerable Plaque Fracture due to Stress-  
848 Induced Debonding Around Cellular Microcalcifications in Thin Fibrous Cap.  
849 *Proceedings of the National Academy of Science* 2006;103:14678-14683.

850 [58] Landau LD, Lifshitz EM. Fluid Mechanics. Second Edition. Volume 6. Butterworth  
851 Heineman. 1987.

- [59] Chau AH, Chan RC, Shishkow M, MacNeill B, Iftimia N, Tearney GJ, Kamm RD, Bouma BE, Kaazempur-Mofrad MR. Mechanical Analysis of Atherosclerotic Plaques Based on Optical Coherence Tomography. *Annals of Biomedical Engineering* 2004;32(11):1494-1503.
- [60] Tovar-Lopez F, Rosengarten G, Khoshmanesh K, Westein E, Jackson SP, Nesbitt WS, Mitchell A. Structural and hydrodynamic simulation of an acute stenosis-dependent thrombosis model in mice. *Journal of Biomechanics* 2011;44(6):1031-1039.
- [61] Owens R. A new microstructure-based constitutive model for human blood. *Journal of non-Newtonian Fluid Mechanics* 2006;140:57-70.
- [62] Mazumdar JN. *Biofluid Mechanics*. World Scientific. 2004.
- [63] Lu J, Zhou X, Raghavan ML. Inverse elastostatic stress analysis in pre-deformed biological structures: Demonstration using abdominal aortic aneurysms. *Journal of Biomechanics*, 2007;40:693–696.
- [64] Holzapfel GA, Gasser TC, Ogden RW. A new constitutive framework for arterial wall mechanics and a comparative study of material models. *Journal of Elasticity*, 2000;61:1–48.
- [65] Krejza J, Arkuszewski M, Kasner SE, Weigle J, Ustymowicz A, Hurst RW, Cucchiara BL, Messe SR. Carotid Artery Diameter in Men and Women and the Relation to Body and Neck Size. *Stroke*, 2006;37:1103-1105.

873 **List of figures and table with caption:**

874

875 Tab. 1: Material and structural parameters of the Holzapfel model describing the  
876 atheromatous plaque components.

877

878 Tab. 2: Spatial convergence: Values of the analysed criteria (see section 2.7) with the degree  
879 of shape functions used in the study ( $P_2$  for  $\mathbf{v}_f$ ,  $P_1$  for  $p$  and  $P_2$  for  $\mathbf{u}_s$ ) and after increasing  
880 the degree of the shape functions ( $P_3$  for  $\mathbf{v}_f$ ,  $P_2$  for  $p$  and  $P_3$  for  $\mathbf{u}_s$ ).

881

882 Tab. 3: Fourier coefficients for the velocity and pressure data.

883

884

885 Fig. 1: Schematic of the model geometry: (A) Domains, boundaries and vector orientation  
886 definition. (B) Schematic of the plaque components. (C) Geometric parameters. (D) 3-D  
887 representation.

888

889 Fig. 2: Curve of the axial velocity at the inlet (a) and of the pressure at the outlet (b) during a  
890 cardiac cycle.

891

892 Fig. 3: (A) Distribution of the von Mises equivalent stress in the plaque and in the healthy  
893 artery upstream and downstream the plaque ( $\sigma^{VM}$ ), using a colour-coded representation on  
894 the deformed shape at systole. It is super-imposed to the shape at diastole, represented in grey.  
895 (A1) Zoom to the top of the stenosis. (A2) Variation of diameter vs. time over a cardiac cycle  
896 for native and stenosed regions of the arteries. (B) Distribution of the longitudinal component  
897 of velocity  $v_z$  represented at systole using a colour-coded representation.

898

899 Fig. 4: Influence of the fibrous cap thickness  $e$  and of material parameters  $k_1^{wall}$  and  $k_1^{cap}$  onto:  
900 (A) the maximum von Mises equivalent stress in the fibrous cap  $\sigma_{max}^{VM}$ . (B) the wall shear  
901 stress (WSS) on the plaque  $\tau_{max}$ . (C) the average radial strain of the plaque  $\varepsilon_R$ . (D) the  
902 average shear strain of the plaque  $\gamma$ . The stenosis severity and the stenosis length are  
903 respectively set to  $S=45\%$  and  $L=10\text{mm}$ .

904

905 Fig. 5: Influence of the stenosis severity  $S$  and the stenosis length  $L$  onto: (A) the maximum  
906 von Mises equivalent stress in the fibrous cap  $\sigma_{max}^{VM}$ . (B) the wall shear stress (WSS) on the  
907 plaque  $\tau_{max}$ . (C) the average radial strain of the plaque  $\varepsilon_R$ . (D) the average shear strain of the  
908 plaque  $\gamma$ . On the left hand side, the stenosis length is set to  $L=10\text{mm}$  and on the right hand  
909 side, the stenosis severity is set to  $S=45\%$ .

910

911 Fig. 6: Mode of deformation and vulnerability of the plaque with respect to stenosis severities  
912  $S$  and lengths  $L$ : (A) Distribution of the von Mises equivalent stress in the fibrous cap ( $\sigma^{VM}$ ),  
913 using a colour-coded representation. The shape at diastole is represented in grey and the stress  
914 distribution is represented on the deformed shape at systole. (B) WSS distribution in the  
915 fibrous cap ( $\tau$ ) using a colour-coded representation on the deformed shape at systole with  
916 velocity vectors.

917

918 Fig. 7: Interactions between the blood and the plaque with flow (A) and without flow (B) for  
919 parameters  $(S,L)=(45\%,10\text{mm})$ : Schematic representation of the plaque deformed by the  
920 pinching effect (A1) and of the plaque deformed by compression without pinching effect  
921 (B1). Pressure distribution around the stenosis using a colour-coded representation (A2) and

922 (B2). Von Mises equivalent stress distribution in the fibrous cap ( $\sigma^{VM}$ ), using a colour-coded  
923 representation (A3) and (B3).

924

925 Fig. 8: Circumferential (a) and longitudinal (b) stress/stretch curves of the healthy artery  
926 model for different material properties tested in the parametric studies and comparison with  
927 the stress/stretch curves of the media and adventitia reported in [50].

928



929    Tab. 1

930

Components	$c$ (kPa)	$k_1$ (kPa)	$k_2$ (-)	$\beta$ (°)
Fibrous cap	78.9	23.7	26.3	0
Healthy artery wall	10.58	24.53	22.13	21
Lipid pool	0.1	0.0	-	-

931

932

933 Tab. 2

934

Finite elements types	$\sigma_{\max}^{VM}$ (kPa)	$\tau_{\max}$ (Pa)	$\varepsilon_R$	$\gamma$
$P_2$ for $\mathbf{v}_f$ , $P_1$ for $p$ and $P_2$ for $\mathbf{u}_s$	384.46	43.254	0.141	0.119
$P_3$ for $\mathbf{v}_f$ , $P_2$ for $p$ and $P_3$ for $\mathbf{u}_s$	384.46	43.312	0.139	0.122

935

936

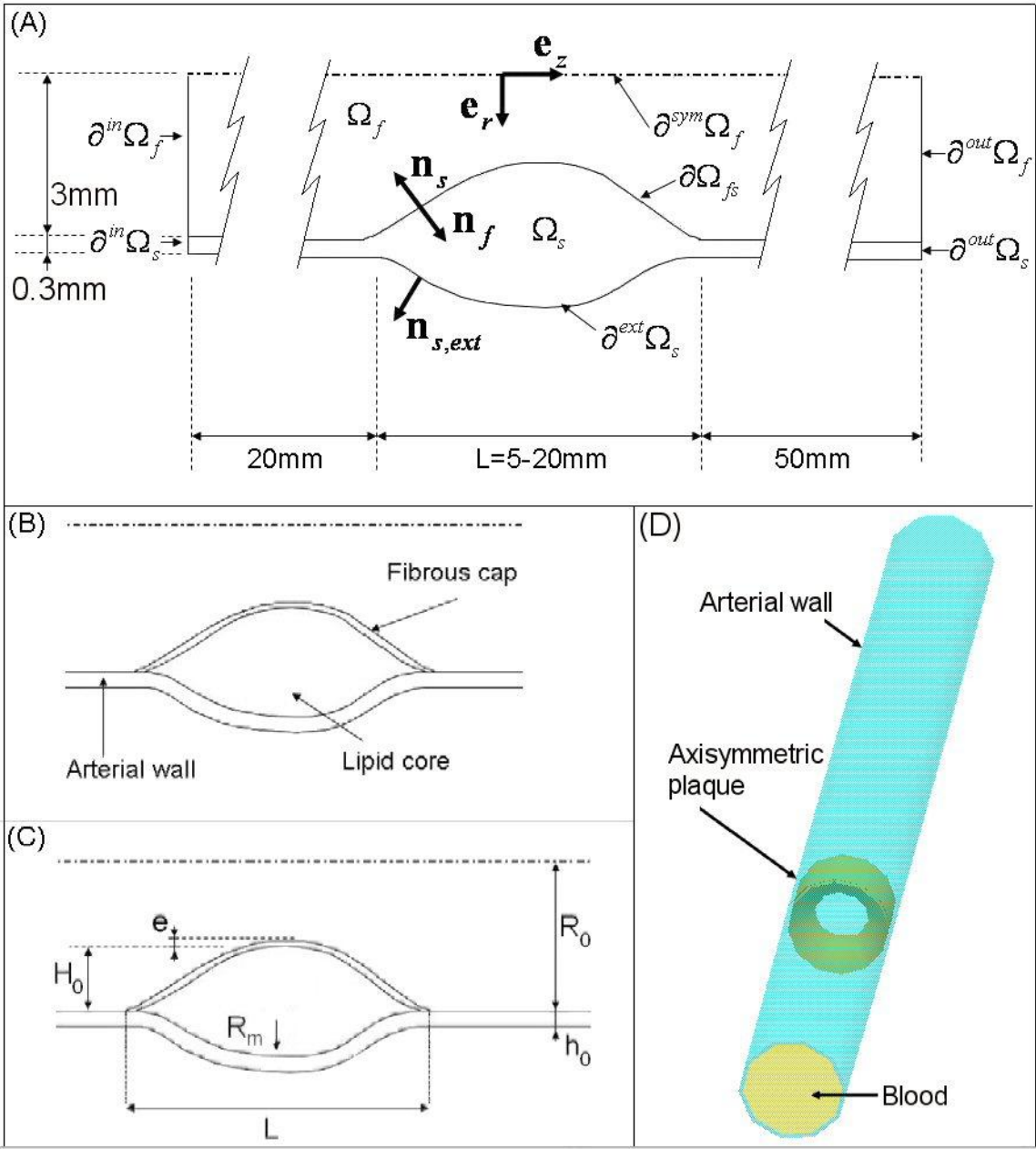
k	$v_k$ (cm/s)	$p_k$ (mmHg)
0	27,8117	93.743
1	-0,1229-11,0224i	-2.4929-12.407i
2	-2,3484+8,5141i	-4.5547-3.3544i
3	5,8539-2,0908i	-2.5546-0.32889i
4	-2,9313-1,1926i	-0.6181+0.45323i
5	1,3812+2,1390i	-0.19113-0.26335i
6	0,7306-0,9195i	-0.79729-0.68989i
7		-0.88357+0.1032i
8		-0.25735+0.22093i
9		-0.37814-0.015991i
10		-0.36849+0.32603i
11		0.015548+0.22243i
12		-0.070833+0.058148i
13		-0.068578+0.13458i
14		0.040223+0.12718i
15		0.030337+0.028246i
16		-0.0060027+0.02907i
17		0.0054199+0.046419i
18		0.0053679+0.0085823i

938

939

940 Fig. 1

941

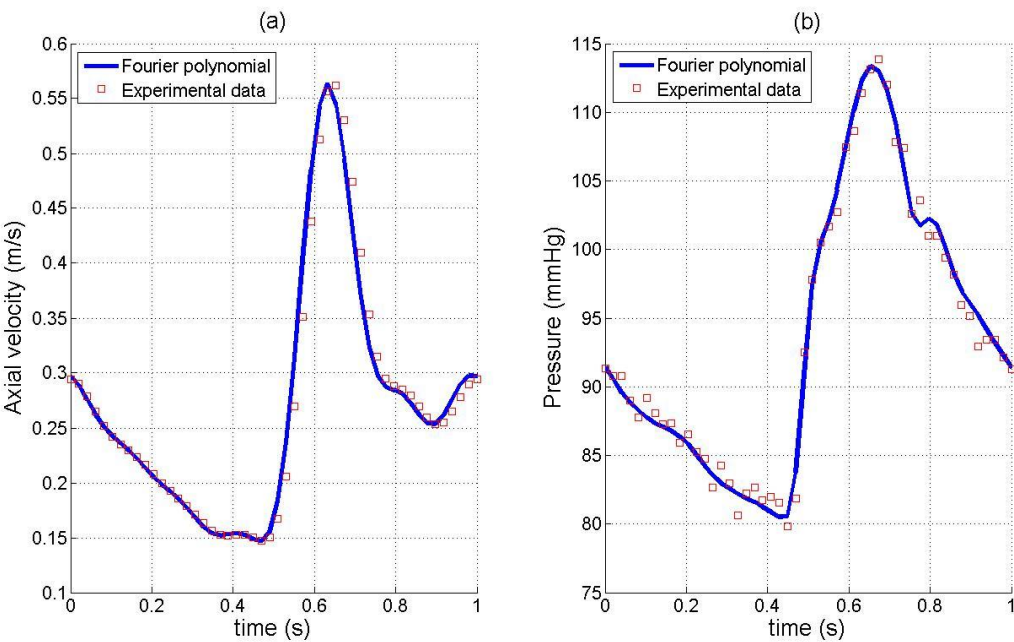


942

943

944 Fig. 2

945

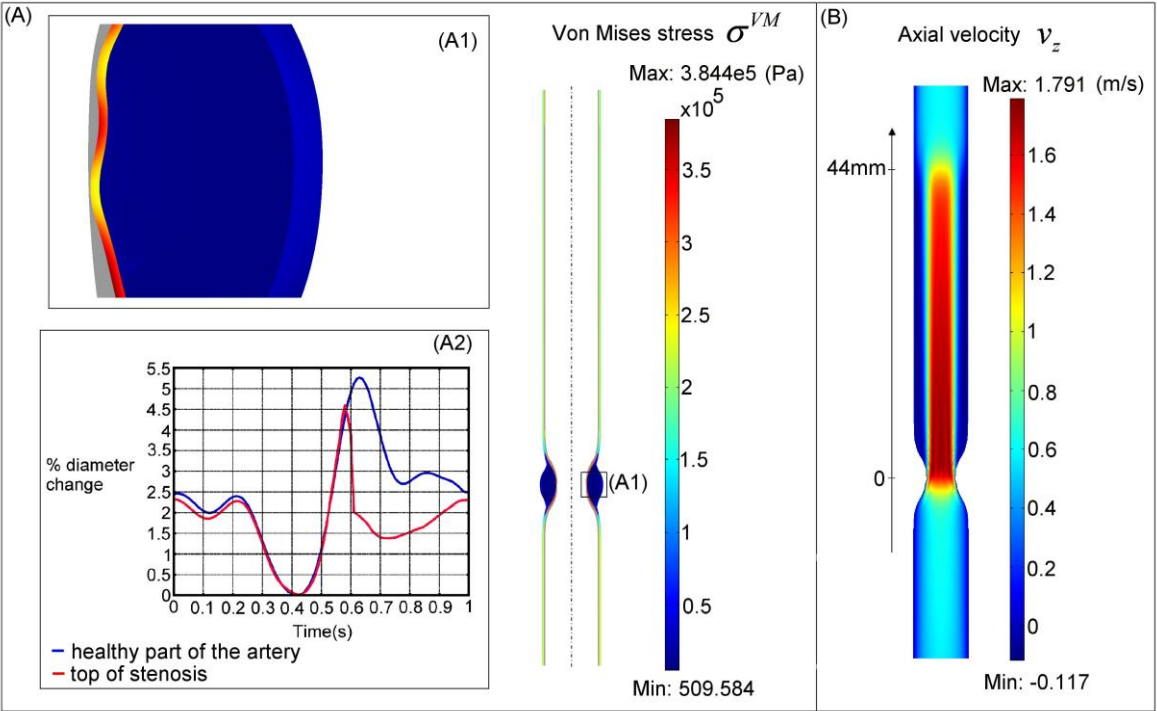


946

947

948 Fig. 3

949

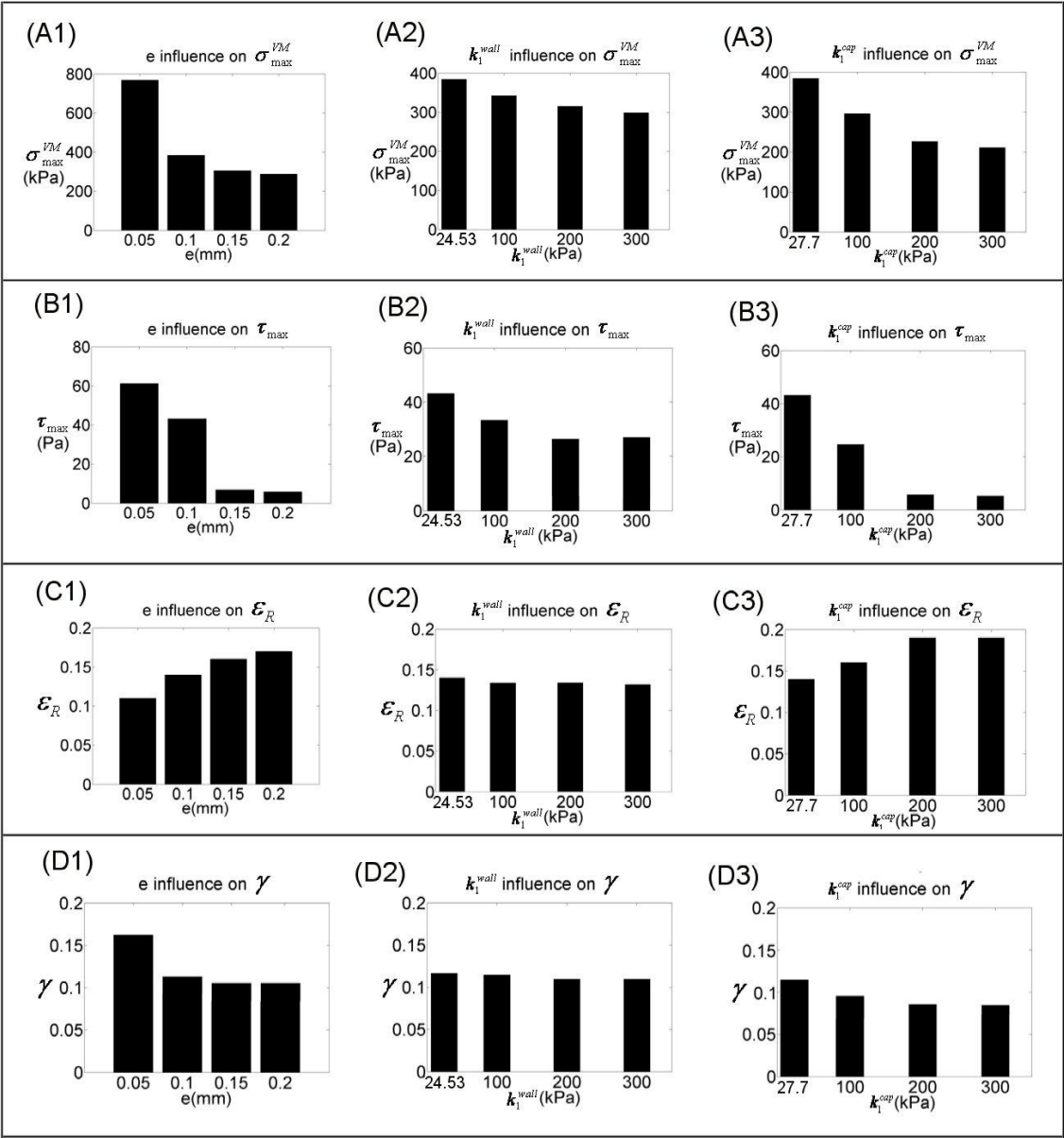


950

951

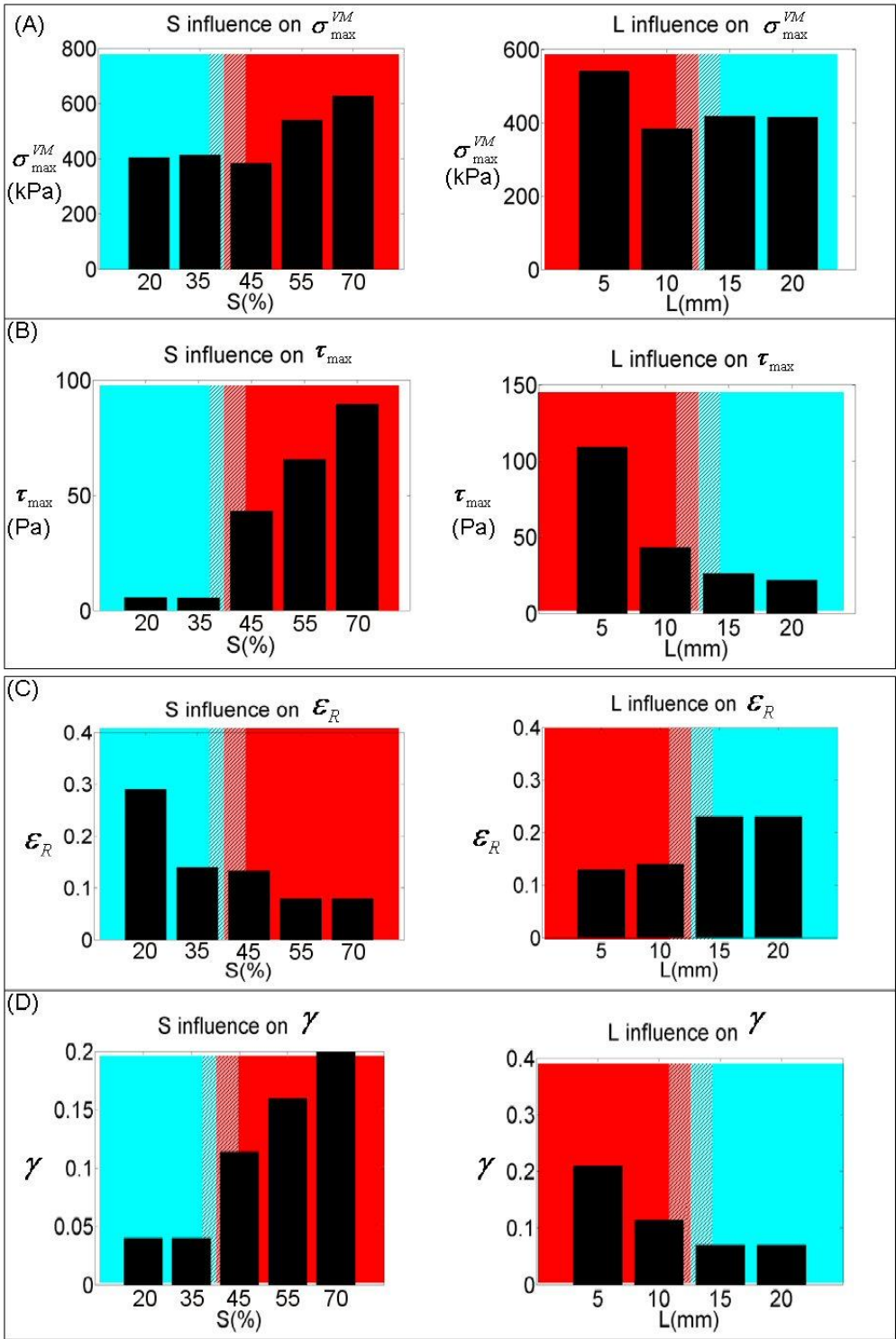
952 Fig. 4

953



954

955

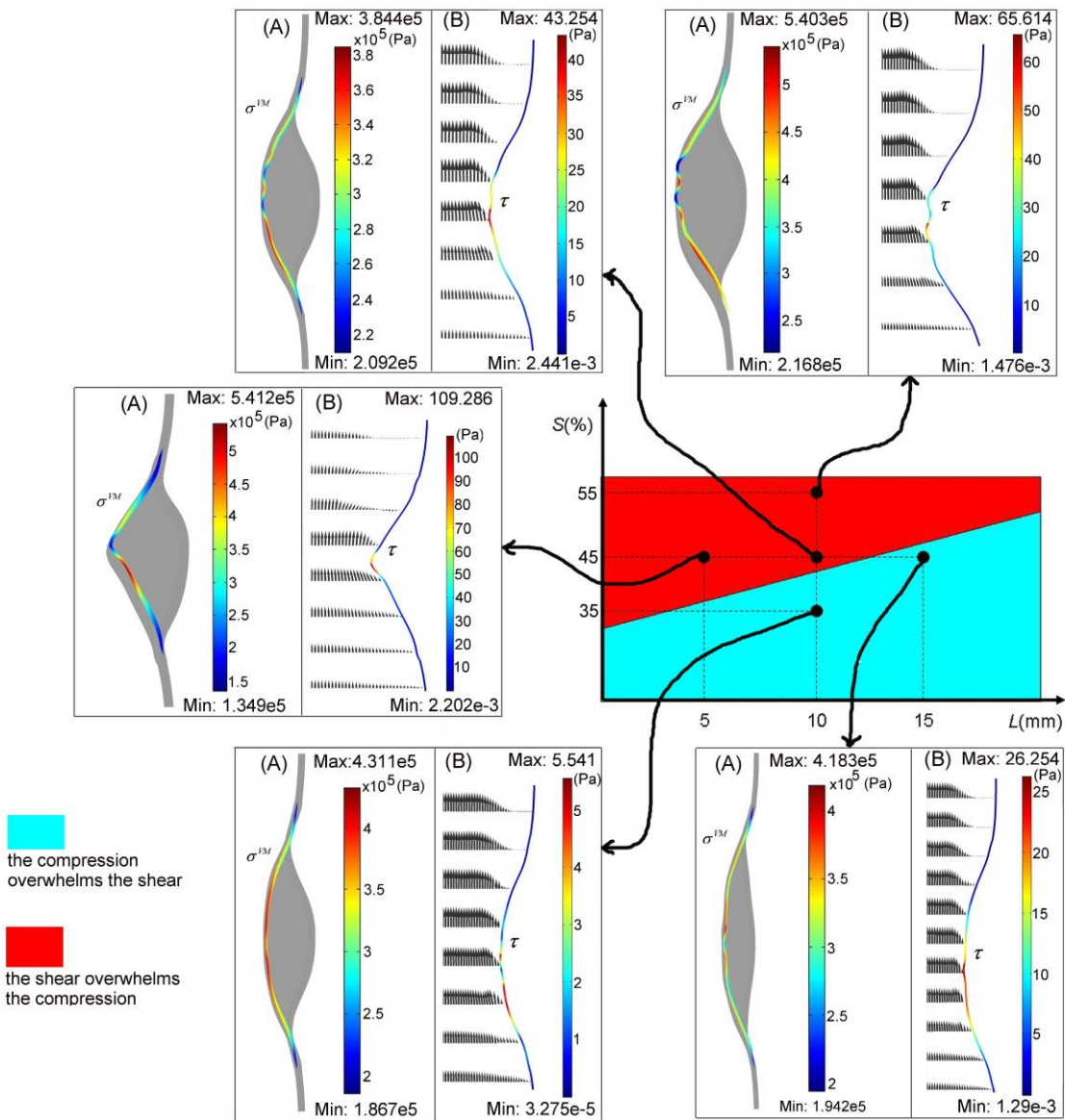


the compression overwhelms the shear  
the shear overwhelms the compression  
transition zone



960 Fig. 6

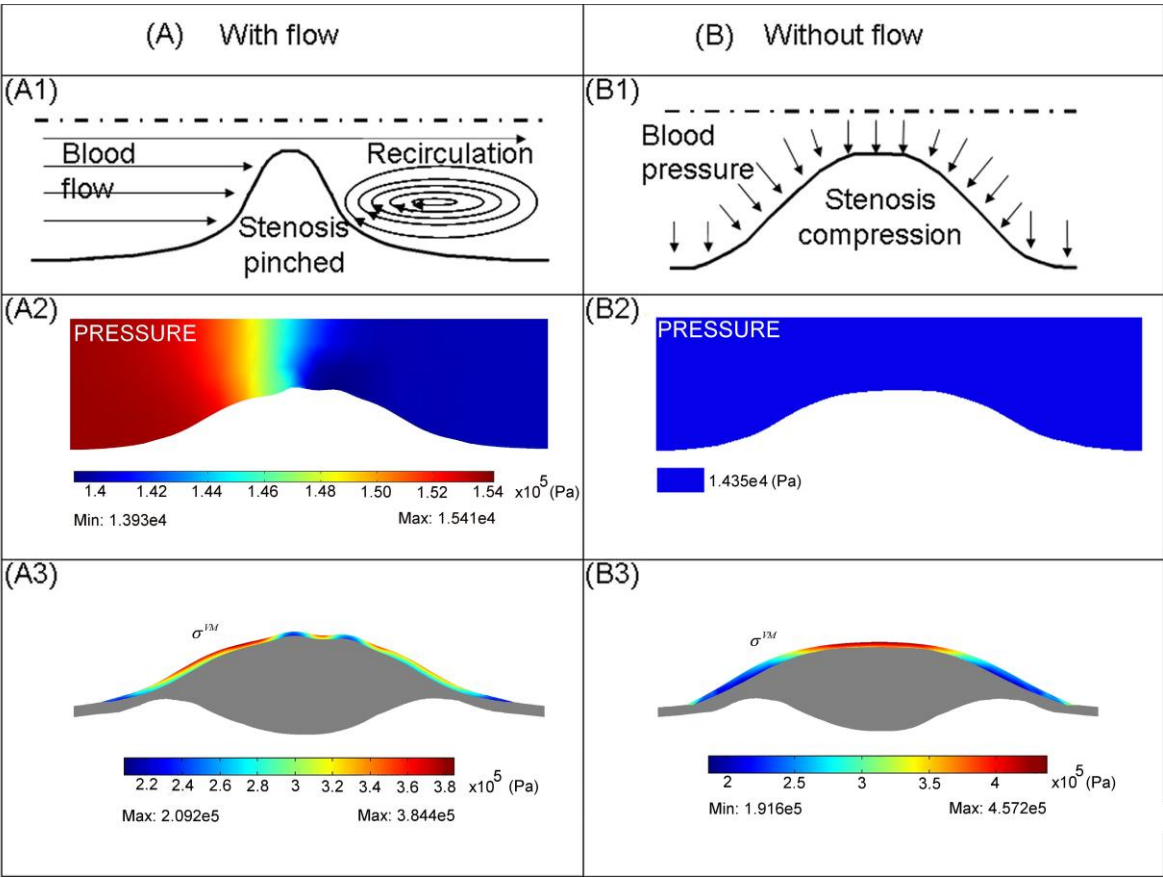
961



962

963

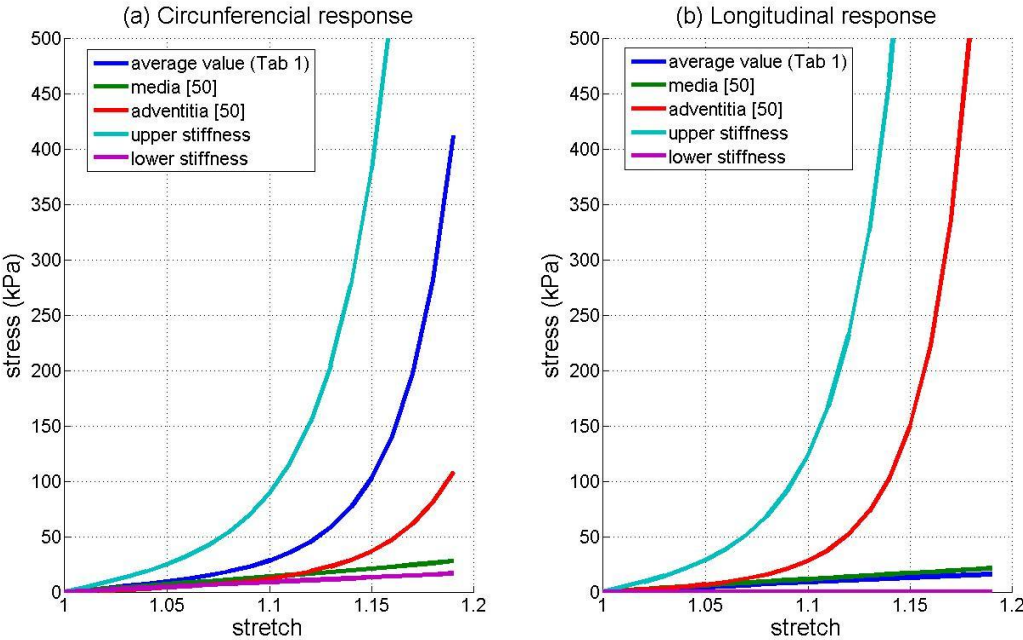
Fig. 7



968 Fig 8

969

970



971